

**Dispersion and decay rate of exciton-polaritons and radiative modes in transition metal dichalcogenide monolayers**

Alpeggiani, Filippo; Gong, Su Hyun; Kuipers, L.

**DOI**

[10.1103/PhysRevB.97.205436](https://doi.org/10.1103/PhysRevB.97.205436)

**Publication date**

2018

**Document Version**

Final published version

**Published in**

Physical Review B

**Citation (APA)**

Alpeggiani, F., Gong, S. H., & Kuipers, L. (2018). Dispersion and decay rate of exciton-polaritons and radiative modes in transition metal dichalcogenide monolayers. *Physical Review B*, 97(20), Article 205436. <https://doi.org/10.1103/PhysRevB.97.205436>

**Important note**

To cite this publication, please use the final published version (if applicable). Please check the document version above.

**Copyright**

Other than for strictly personal use, it is not permitted to download, forward or distribute the text or part of it, without the consent of the author(s) and/or copyright holder(s), unless the work is under an open content license such as Creative Commons.

**Takedown policy**

Please contact us and provide details if you believe this document breaches copyrights. We will remove access to the work immediately and investigate your claim.

## Dispersion and decay rate of exciton-polaritons and radiative modes in transition metal dichalcogenide monolayers

Filippo Alpegiani, Su-Hyun Gong, and L. Kuipers

*Kavli Institute of Nanoscience, Department of Quantum Nanoscience, Delft University of Technology,  
Lorentzweg 1, 2628 CJ Delft, The Netherlands*



(Received 16 October 2017; revised manuscript received 2 May 2018; published 22 May 2018)

The two-dimensional excitons of transition metal dichalcogenide (TMDC) monolayers make these materials extremely promising for optical and optoelectronic applications. When the excitons interact with the electromagnetic field, they will give rise to exciton-polaritons, i.e., modes that propagate in the material plane while being confined in the out-of-plane direction. In this work, we derive the characteristic equations that determine both radiative and polaritonic modes in TMDC monolayers and we analyze the dispersion and decay rate of the modes. The condition for the existence of exciton-polaritons can be described in terms of a strong-coupling regime for the interaction between the exciton and the three-dimensional continuum of free-space electromagnetic modes. We show that the threshold for the strong-coupling regime critically depends on the interplay between nonradiative losses and the dielectric function imbalance at the two sides of the monolayer. Our results illustrate that a fine control of the dielectric function of the embedding media is essential for realizing exciton-polaritons in the strong-coupling regime.

DOI: [10.1103/PhysRevB.97.205436](https://doi.org/10.1103/PhysRevB.97.205436)

### I. INTRODUCTION

Transition metal dichalcogenides (TMDCs) are layered materials that can be easily exfoliated into stable monolayer structures of single-atom thickness [1]. In this way, they can represent a prototypical two-dimensional material, like graphene and other two-dimensional crystals [2,3]. Due to the lack of in-plane inversion symmetry and a strong spin-orbit effect, it is possible to finely control the distribution of electrons at nondegenerate points in reciprocal space, establishing an ideal platform for valleytronic applications [4,5]. Moreover, TMDC monolayers provide a promising framework for constructing qubits [6] or topological polaritonic states [7].

TMDC monolayers are direct-gap semiconductors with the gap located at the  $K$  and  $K'$  points in the first Brillouin zone. One of the most striking properties is the presence of exceptionally strong excitons which dominate the response of the monolayer in the optical range. Such excitons are characterized by extremely high binding energies, even exceeding a few hundred of meV, which allow the excitons to persist even at room temperature [8–16]. For these reasons, TMDC monolayers have attracted a major amount of interest in view of developing novel optical and optoelectronic devices [17], for instance, in fields such as photovoltaics [18], photodetection [19,20], or light emission [10,21].

In the context of semiconductor quantum wells, it was demonstrated long ago that the quasi-two-dimensional excitons interact with the electromagnetic field and give rise to *exciton-polaritons*, i.e., hybrid light-matter modes with an evanescent field in the out-of-plane direction [22–25]. The existence of similar polaritonic modes for TMDC monolayers has been recently predicted by Khurgin [26]. It is essential to note that these exciton-polaritons are different from the cavity-polaritons which are obtained by confining the electromagnetic field within a two-dimensional cavity. Cavity-polaritons,

which have been also recently realized for TMDC monolayers [27,28], are based on the reversible exchange of energy between the exciton and a single confined electromagnetic mode. Conversely, exciton-polaritons are collective modes that originate from the interaction between the exciton and the continuum of three-dimensional electromagnetic modes. Similarly to surface plasmon polaritons, their evanescent character is due to the momentum mismatch with free-space electromagnetic radiation: being located outside of the light cone in frequency-momentum space, they cannot be directly converted into three-dimensional photons [25].

In light of these considerations, it is clear that, in the spectrum of two-dimensional systems, confined polaritonic modes always coexist with *radiative modes* (or quasinormal modes), which lie inside the light cone. Radiative modes are characterized by a complex frequency, with the imaginary part representing the intrinsic radiative decay rate, and they correspond to the resonances that are typically observed in the transmission or reflection spectrum of the system. Exciton-polaritons, on the other hand, despite being dark to far-field optical measurements, can be probed by evanescent waves generated in the Otto configuration [29], with near-field experiments [30], or by means of suitable gratings [31].

As it has been pointed out in the case of semiconductor quantum wells for both interband [32] and intersubband [33,34] transitions, coherence plays an essential role for the formation of the exciton-polariton. In the presence of an additional nonradiative decay channel, whose existence is to be expected in any realistic system, the dispersion and the characteristics of the exciton-polariton are not only quantitatively but also qualitatively affected by the magnitude of the incoherent losses. A sufficiently high value of nonradiative losses triggers a transition from the strong-coupling regime of light-matter interaction, characterized by the emergence of mixed excitonic-electromagnetic modes, to the weak-coupling

regime, where the exciton is only perturbatively affected by the coupling with light. Therefore, it is critical to accurately determine the effect of nonradiative losses on the dispersion and the decay rate of the modes in view of exploiting exciton-polaritons in TMDC monolayers for optoelectronic applications.

There are other important characteristics that differentiate TMDC monolayers from traditional semiconductor heterostructures. For instance, since TMDC monolayers are typically exfoliated on a substrate, there may be a large dielectric function imbalance between the two embedding optical media on the two sides of the monolayer, which is also expected to play a significant role on the electrodynamics of the system. All these effects need to be taken into account in order to fully understand the properties of the electromagnetic modes.

In this work, we present a thorough theoretical analysis of the dispersion and the decay rate of both polaritonic and radiative modes in TMDC monolayers, as a function of the nonradiative loss rate and dielectric function imbalance. Radiative and polaritonic modes are the solutions of the same master equation and they are classified according to the spatial profile of the associated electromagnetic field. We show that, for nonzero nonradiative losses, an additional ‘‘anomalous’’ dissipation-induced polariton appears. The presence of this additional mode is crucial for understanding the strong-weak coupling transition, when it merges with the ‘‘ordinary’’ exciton-polariton. In order to obtain a complete picture of the nature of radiative and polaritonic modes in TMDC monolayers, we perform a parametric study of the modal dispersion by taking the nonradiative decay rate and the dielectric function imbalance, i.e., the ratio between the dielectric functions of the claddings, as free parameters. We demonstrate that in the presence of a large dielectric function imbalance on the two surfaces of the monolayer, the maximum amount of nonradiative losses compatible with the existence of the strong-coupling regime is much lower than in the symmetric case. These results indicate that a very fine control of the dielectric function of the embedding media is essential for maximizing the effectiveness of exciton-polariton-based applications.

The work is organized as follows. In Sec. II, we derive the master equation for both radiative and polaritonic modes in TMDC monolayers. In Sec. III, we analyze the dispersion and the decay rate of the modes for the illustrative example of tungsten disulfide (WS<sub>2</sub>). Finally, in Sec. IV, we study the variation of the modal dispersion as a function of the nonradiative decay rate and dielectric function imbalance, in view of elucidating the mechanism of the transition from the strong-coupling to the weak-coupling regimes.

## II. CHARACTERISTIC EQUATION

Transition metal dichalcogenide monolayers are direct-gap semiconductors with the band gap located at the  $K$  and  $K'$  points in the first Brillouin zone [1,17]. Here and in the following, we assume that the  $z$  axis of the system is oriented perpendicularly to the monolayer plane (coinciding with the  $c$  axis of the unit cell). The wave function of the electrons in the monolayer has a finite spatial extent along the out-of-plane direction of the order of the lattice constant  $c$ . The dielectric function of the monolayer can be calculated from the electron density response function within the well-established

formalism of linear response theory [35]. As the system is not translational invariant, the ‘‘microscopic’’ dielectric function is necessarily nonlocal, i.e.,  $\varepsilon = \varepsilon(\mathbf{r}, \mathbf{r}', \omega)$ . The constitutive relation for the electric displacement field can be equivalently written in terms of the nonlocal tensor susceptibility  $\overline{\overline{\chi}}^{(\text{ex})}(z, z', \omega)$  as follows [25]:

$$\mathbf{D}(z, \omega) = \varepsilon_0 \left[ \overline{\overline{\varepsilon}}_b \mathbf{E}(z, \omega) + \int dz' \overline{\overline{\chi}}^{(\text{ex})}(z, z', \omega) \mathbf{E}(z', \omega) \right], \quad (1)$$

with  $\overline{\overline{\varepsilon}}_b$  being the background dielectric function. Such nonlocal susceptibility tensor can be computed with *ab initio* techniques [35].

In order to avoid the complications of a specific microscopic model, in this work we will employ a mean-field approximation [36]. We model the response of the exciton with an effective *local* dielectric tensor  $\overline{\overline{\varepsilon}}^{(\text{eff})}(\omega)$ , whose features are described in terms of phenomenological parameters that can be experimentally determined. Such approximation is justified since the thickness of the dichalcogenide layer in the  $c$ -axis direction,  $L$ , is much smaller than the wavelength of interest ( $L \ll \lambda$ ).

In the following, we will briefly summarize how such mean-field approximation is derived, following the approach of Ref. [36]. It has been shown that the traditional Wannier-Mott model provides a good starting point for describing excitons in TMDC monolayers [37]. Following the well-established theory of Wannier-Mott excitons in two-dimensional semiconductor nanostructures [25,36], we can write the nonlocal tensor susceptibility of the system in the following form:

$$\overline{\overline{\chi}}^{(\text{ex})}(z, z', \omega) = \frac{1}{\hbar} \sum_{\alpha} \frac{2g_{\alpha}\omega_{\alpha}(\boldsymbol{\mu}_{vc}^* \otimes \boldsymbol{\mu}_{vc})|F_{\alpha}(0)|^2}{(\omega_{\alpha} - i\gamma_{\alpha}/2)^2 - \omega^2} \xi_{\alpha}(z)\xi_{\alpha}(z'). \quad (2)$$

In this equation, the sum runs over all excitons with energies  $\hbar\omega_{\alpha}$  and Wannier-Mott envelope functions  $F_{\alpha}(\mathbf{r}_{\parallel})$ . Each exciton is characterized by an intrinsic nonradiative decay rate  $\gamma_{\alpha}$ . Recent experiments suggest that nonradiative losses are mostly determined by phonon-induced intravalley scattering and intervalley scattering into dark states [38,39]. In our model, the nonradiative decay rate is treated as a phenomenological parameter and incorporated as an imaginary part for the exciton frequency. The symbol  $\boldsymbol{\mu}_{vc}$  indicates the dipole matrix element of the valence-conduction band transition, whereas the current term  $\xi_{\alpha}(z) = u_c(z)u_v(z)$  is the product of the  $c$ -axis confinement functions  $u_v$  and  $u_c$  for electrons in the valence and conduction bands, respectively. The symbol  $g_{\alpha}$  is a spin-orbit factor. For simplicity, we have explicitly written only the excitonic contribution to the optical response of the system. We assume that all additional contributions, including, for instance, those originating from the continuum of electronic interband transitions, are included into the local background dielectric function  $\overline{\overline{\varepsilon}}_b$ .

The dipole matrix element determines whether excitons with a given polarization can couple with light, according to optical selection rules for interband transitions. In-plane polarized excitons have a dipole moment

$$\boldsymbol{\mu}_{vc} \propto \tau \hat{\mathbf{x}} + i\hat{\mathbf{y}}, \quad (3)$$

where  $\tau$  ( $\tau = \pm 1$ ) is the valley index designating the inequivalent  $K$  and  $K'$  points in the first Brillouin zone [37].

These excitons are associated with the resonances observed in normal-incidence spectroscopy or luminescence [9,10,12,13]. Moreover, TMDC monolayers also support out-of-plane polarized excitons, which can be detected with an edge collection setup [16]. As a result of the splitting between the lowest-energy conduction bands (which is due to the lack of inversion symmetry in the unit cell), out-of-plane polarized excitons have different energies with respect to in-plane ones because they originate from different interband transitions [16,40].

At this point, we can apply the mean-field approximation. We treat the in-plane and the out-of-plane polarized excitons separately. Following Ref. [36], we define the effective local (anisotropic) dielectric function for the dichalcogenide medium as the ratio between the in-plane space-averaged electric displacement vector and the in-plane space-averaged electric field  $\varepsilon_p(\omega) = D_p^{(\text{av})}(\omega)/E_p^{(\text{av})}(\omega)$  ( $p = \parallel, z$ ).

In the case of the in-plane polarized exciton, we can approximate the in-plane electric field in the layer with its average over the layer thickness, i.e.,  $\mathbf{E}_{\parallel}(z, \omega) \simeq \mathbf{E}_{\parallel}^{(\text{av})}(\omega) = (1/L) \int_L dz \mathbf{E}_{\parallel}(z, \omega)$ . In this way, we can pull out the electric field term from the integral in Eq. (1). By further taking the spatial average of Eq. (1) over the layer, we are led to the result for the in-plane effective dielectric function

$$\begin{aligned} \varepsilon_{\parallel}^{(\text{eff})}(\omega) &= \varepsilon_{b\parallel} + \frac{c}{L} \sum_{\alpha} \frac{2g_{\alpha}\omega_{\alpha}(\mu_{vc}^{\parallel})^2 |F(0)|^2 \left| \int dz \xi(z) \right|^2}{\hbar c [(\omega_{\alpha} - i\gamma_{\alpha}/2)^2 - \omega^2]} \\ &= \varepsilon_{b\parallel} + \frac{c}{L} \sum_{\alpha} \frac{\Gamma_{\alpha}^{\parallel}}{(\omega_{\alpha} - i\gamma_{\alpha}/2)^2 - \omega^2}, \end{aligned} \quad (4)$$

where the last term serves as a definition of the ‘‘bare’’ exciton radiative rate  $\Gamma_{\alpha}^{\parallel}$ .

The situation is different for the out-of-plane polarization. In this case, the electric displacement field is continuous across the monolayer interfaces, i.e.,  $D_z(z, \omega) \simeq D_z^{(\text{av})}(\omega)$ . By defining  $p_{\alpha}(\omega) = \int dz \xi_{\alpha}(z) E_z(z, \omega)/D_z^{(\text{av})}(\omega)$ , multiplying Eq. (1) by  $\xi_{\alpha}(z)$ , and integrating along  $z$ , we obtain the linear system of equations

$$\int dz \xi_{\alpha} = \varepsilon_0 \varepsilon_{bz} p_{\alpha} + \sum_{\beta} \frac{2g_{\beta}\omega_{\beta}\varepsilon_0(\mu_{vc}^z)^2 |F(0)|^2}{\hbar [(\omega_{\beta} - i\gamma_{\beta}/2)^2 - \omega^2]} I_{\alpha\beta} p_{\beta}, \quad (5)$$

with  $I_{\alpha\beta} = \int dz \xi_{\alpha}(z)\xi_{\beta}(z)$ . This linear system needs to be solved in order to retrieve the effective out-of-plane dielectric function

$$\frac{1}{\varepsilon_z^{(\text{eff})}(\omega)} = \frac{1}{\varepsilon_{bz}} - \frac{\varepsilon_0}{L} \sum_{\alpha} \frac{2g_{\alpha}\omega_{\alpha}(\mu_{vc}^z)^2 |F(0)|^2 \int dz \xi(z)}{\varepsilon_{bz} \hbar [(\omega_{\alpha} - i\gamma_{\alpha}/2)^2 - \omega^2]} p_{\alpha}(\omega). \quad (6)$$

There is an important qualitative difference between the in-plane and the out-of-plane polarizations. In the in-plane case, the resonances in the effective dielectric function correspond to the exciton energies, as it is clear from Eq. (4). Conversely, in the out-of-plane case, the optical resonances are shifted in frequency with respect to the ‘‘bare’’ exciton energies. This fact can be easily illustrated by considering the situation where only a single out-of-plane polarized exciton is present. The application of Eqs. (5) and (6) leads us to the effective out-of-

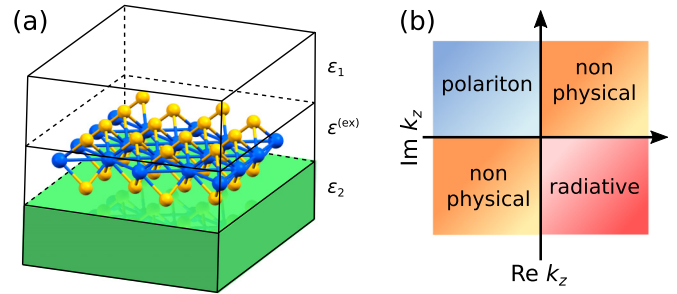


FIG. 1. (a) Scheme of the system considered in this work: a TMDC monolayer, modeled with an effective dielectric tensor, is interposed between air and a dielectric substrate, with dielectric constants  $\varepsilon_1$  and  $\varepsilon_2$ , respectively. (b) Classification of the electromagnetic modes according to the sign of the real and imaginary parts of the out-of-plane wave vector  $k_z$ .

plane dielectric function

$$\begin{aligned} \frac{1}{\varepsilon_z^{(\text{eff})}(\omega)} &= \frac{1}{\varepsilon_{bz}} \left[ 1 - \frac{c}{L} \frac{2g_{\alpha}\omega_{\alpha}(\mu_{vc}^z)^2 |F(0)|^2 \int dz \xi(z)}{\varepsilon_{bz} \hbar c [(\omega_{\alpha} - i\gamma_{\alpha}/2)^2 + \Delta_{\alpha}^2 - \omega^2]} \right] \\ &= \frac{1}{\varepsilon_{bz}} - \frac{c}{L} \frac{\Gamma_{\alpha}^z}{(\omega_{\alpha} - i\gamma_{\alpha}/2)^2 + \Delta_{\alpha}^2 - \omega^2}, \end{aligned} \quad (7)$$

where again the second equation serves as a definition for the exciton coupling constant  $\Gamma_{\alpha}^z$ . The squared frequency of the resonance is adjusted with respect to the bare exciton value  $\omega_{\alpha}^2$  by the term

$$\Delta_{\alpha}^2 = 2g_{\alpha}\omega_{\alpha}(\mu_{vc}^z)^2 |F(0)|^2 I_{\alpha\alpha} / (\hbar \varepsilon_{bz}), \quad (8)$$

which is sometimes called the *depolarization shift* [24]. The same term is responsible for the experimentally observed splitting between the in-plane and out-of-plane exciton-polaritons in centrosymmetric semiconductor quantum wells, where the exciton transition frequencies for the two polarizations would be degenerate without it [25,36].

We consider a TMDC monolayer interposed between two semi-infinite half-spaces with dielectric constants  $\varepsilon_1$  and  $\varepsilon_2$ , respectively, as sketched in Fig. 1(a). Following the mean-field theory discussed above, the system can be described with a stratified local dielectric tensor of the form

$$\bar{\varepsilon}(z, \omega) = \begin{cases} \bar{I}\varepsilon_1, & z < z_0 - L/2 \\ \bar{I}\varepsilon_2, & z > z_0 + L/2 \\ \bar{\varepsilon}^{(\text{eff})}(\omega), & \text{otherwise} \end{cases} \quad (9)$$

where the monolayer effective susceptibility takes the value in Eq. (4), i.e.,  $\bar{\varepsilon}^{(\text{eff})}(\omega) = (\bar{I} - \hat{\mathbf{z}}\hat{\mathbf{z}})\varepsilon_{\parallel}^{(\text{eff})}(\omega)$ , or in Eq. (6),  $\bar{\varepsilon}^{(\text{eff})}(\omega) = (\hat{\mathbf{z}}\hat{\mathbf{z}})\varepsilon_z^{(\text{eff})}(\omega)$ , according to the exciton polarization.

Following the ‘‘quasiparticle’’ approach in the terminology of Ref. [41], we mathematically define the electromagnetic *modes* of the system as the complex-frequency solutions of the characteristic wave equation for the electric field

$$\nabla \times \nabla \times \mathbf{E}(\mathbf{r}, \omega) - \bar{\varepsilon}(z, \omega) \frac{\omega^2}{c^2} \mathbf{E}(\mathbf{r}, \omega) = 0 \quad (10)$$

with outgoing boundary conditions for  $|z| \rightarrow \infty$ . Due to the translational invariance in the  $xy$  plane, we look for solutions of the form  $E(\mathbf{r}, \omega) = \mathcal{E}(z, k_{\parallel}, \omega) e^{i\mathbf{k}_{\parallel} \cdot \mathbf{r}_{\parallel}}$  and classify the solutions according to the (real) in-plane wave vector  $\mathbf{k}_{\parallel}$ . The wave equation can be solved numerically by using, for instance, the transfer matrix method [42], as it is well established for stratified systems. Note that our definition of a mode is very general, and in some cases (discussed in the following) it will be applied to strongly dispersionless states, which do not always adhere to the intuitive picture of an electromagnetic mode. Nevertheless, such modes represent mathematically well-defined constructs, which provide a viable description of light–matter interaction in the system. In particular, for all the modes calculated in this work, the imaginary part of the frequency is smaller than the real part [ $\text{Im}(\omega)/\text{Re}(\omega) \simeq 1/100$ ], justifying the validity of the quasiparticle picture.

The characteristic equation for electromagnetic modes can be further simplified without significant loss of accuracy to an analytical expression which is particularly convenient for illustrative purposes. To this end, we will limit ourselves to the case of a single exciton with energy  $\hbar\omega_0$ . Furthermore, in the case of in-plane polarized excitons, since the thickness of the TMDC layer is much smaller than the wavelength of the system, we can make a further simplification by adopting a current-sheet approximation, i.e., by modeling the monolayer as an infinitely thin sheet with an excitonic surface current

$$\boldsymbol{\sigma}_{\parallel}(\omega) = i\omega\epsilon_0 \frac{c\Gamma_0^{\parallel}}{(\omega_0 - i\gamma_0/2)^2 - \omega^2} \mathbf{E}_{\parallel}(z_0, \omega). \quad (11)$$

This latter approximation allows us to neglect the effect of the background dielectric function of the TMDC, while, at the same time, preserving all the relevant physics of the light–exciton interaction.

The interaction of in-plane polarized excitons with light gives rise to two different families of electromagnetic modes: *T modes*, with the exciton dipole momentum transverse to the in-plane wave vector  $\mathbf{k}_{\parallel}$  (corresponding to transverse electric, or TE, modes) and *L modes*, with the dipole momentum parallel to  $\mathbf{k}_{\parallel}$  (corresponding to transverse magnetic, or TM, modes). By using the single-exciton and current-sheet approximations and enforcing the boundary conditions for the  $H_z$  component of the magnetic field at the interfaces, we obtain the characteristic equations for the *T* modes (TE polarized):

$$[(\omega_0 - i\gamma_0/2)^2 - \omega^2](ck_{z1} + ck_{z2}) - i\omega^2\Gamma_0^{\parallel} = 0. \quad (12)$$

Similarly, from the boundary conditions of the in-plane electric field, we derive the characteristic equation for the *L* modes (TM polarized):

$$[(\omega_0 - i\gamma_0/2)^2 - \omega^2] \left( \frac{\epsilon_1}{ck_{z1}} + \frac{\epsilon_2}{ck_{z2}} \right) - i\Gamma_0^{\parallel} = 0. \quad (13)$$

Out-of-plane polarized excitons only couple with the  $z$  component of the light field, generating *Z modes* with TM polarization. In this case, however, due to the out-of-plane polarization of the excitons, we cannot use the current-sheet approximation, but we have to take into account the finite extension of the internal charge distribution of the electrons. In order to obtain a simplified characteristic equation, we can apply the nonlocal theory developed in Ref. [33] in the

long-wavelength approximation. In this way, we are led to the expression for *Z* modes:

$$[(\omega_0 - i\gamma_0/2)^2 + \Delta_0^2 - \omega^2] \left( \frac{k_{z1}}{\epsilon_1} + \frac{k_{z2}}{\epsilon_2} \right) - ic k_{\parallel}^2 \Gamma_0^z = 0, \quad (14)$$

where  $\Delta_0^2$  is the exciton depolarization shift [Eq. (8)]. In all these equations, we define  $k_{zj} = (\epsilon_j \omega^2 / c^2 - k_{\parallel}^2)^{1/2}$  ( $j = 1, 2$ ).

This set of equations allows us to investigate the general properties of the electromagnetic modes of the system from a simple and analytical model. As it has been stressed in previous work [32], it is crucial to note that the very same characteristic equations nonperturbatively describe both polaritonic (i.e., spatially confined) and radiative (i.e., spatially diverging) states. The distinction between the two families of modes lies in the complex out-of-plane wave vectors  $k_{zj} = (\epsilon_j \omega^2 / c^2 - k_{\parallel}^2)^{1/2}$  in the two extremal semi-infinite layers ( $j = 1, 2$ ). Assuming a temporal and spatial dependence for the field of the form  $\mathbf{E} \propto e^{i(\mathbf{k}_{\parallel} \cdot \mathbf{r}_{\parallel} + ik_{zj}z - \omega t)}$ , modes with  $\text{Im} k_{zj} \geq 0$  and  $\text{Re} k_{zj} \leq 0$  represent exponentially decaying polaritonic states, whereas modes with  $\text{Im} k_{zj} < 0$  and  $\text{Re} k_{zj} > 0$  correspond to exponentially diverging radiative states. The remaining cases represent unphysical modes with  $\text{Im} \omega > 0$ , which must be excluded on grounds of energy conservation for passive media [32,33]. The classification of the modes according to the sign of the real and imaginary parts of  $k_z$  is summarized in Fig. 1(b). As a result, Eqs. (12)–(14) provide us with a full characterization of the spectrum of the TMDC monolayer. As it is expected for two-dimensional systems, the complex-frequency solutions encompass both polaritonic and radiative modes.

### III. RADIATIVE AND POLARITONIC MODES

In general, out-of-plane polarized interband transitions in TMDC monolayers are much weaker than in-plane polarized ones because they are based on spin-orbit-interaction–induced band mixing. From theoretical considerations, the authors of Ref. [16] estimate a ratio between the corresponding radiative strengths of the order of  $\Gamma^z / \Gamma^{\parallel} \sim 10^{-4} - 10^{-2}$ . For this reason, in the following we will focus exclusively on in-plane polarized excitons, which are the most promising for technological applications. We limit ourselves to a single in-plane polarized exciton of energy  $\hbar\omega_0$ , to be identified, for all practical purposes, with the so-called “A” exciton that dominates the optical response of TMDC monolayers [43]. For the sake of completeness, the results for out-of-plane polarized excitons are presented in the Appendix.

As an illustrative example, we will focus on WS<sub>2</sub>. The effective dielectric constant is reported in Ref. [43] from reflectance measurements on monolayered samples. We can directly compare our Eq. (4) with the experimental data in order to estimate the value of the parameters. The experiments evidence the presence of a Lorentzian peak associated to the “A” exciton with an energy  $\hbar\omega_0 = 2.014$  eV and a width  $\hbar\gamma_0 = 0.029$  eV [43]. From the reported oscillator strength of the peak ( $f_0 = 1.9$  eV<sup>2</sup>) and the layer thickness assumed in the fit ( $L = 6.18$  Å), we derive, by applying Eq. (4), a radiative rate  $\hbar\Gamma_0^{\parallel} = f_0 L / (\hbar c) \simeq 6$  meV.

As a starting point, we consider the symmetric configuration of a WS<sub>2</sub> monolayer suspended in air ( $\epsilon_1 = \epsilon_2 = 1$ ). The

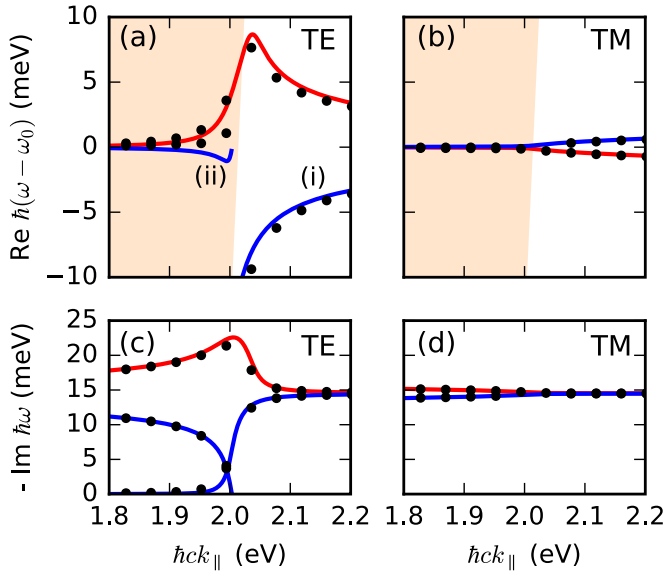


FIG. 2. (a), (b) Real part and (c), (d) imaginary part of the frequency dispersion of the electromagnetic modes of a TMDC monolayer, as a function of the in-plane wave vector. The red lines, corresponding to in-plane radiative modes, and the blue lines, corresponding to in-plane polariton modes, have been computed from Eqs. (12) and (13) for TE polarized *T modes* (a), (c) and TM polarized *L modes* (b), (d). The shaded region marks the light cone. The parameters are  $\hbar\omega_0 = 2.014$  eV,  $\hbar\gamma_0 = 0.029$  eV,  $\hbar\Gamma_0^\parallel = 6$  meV,  $\varepsilon_1 = \varepsilon_2 = 1$ , corresponding to  $\text{WS}_2$  in a symmetric configuration. The dots indicate the results of a full-wave numerical calculation of the modal frequencies using the experimentally determined dielectric constant of  $\text{WS}_2$  [43].

dispersion of the real and the imaginary parts of the complex frequencies of TE electromagnetic modes (*T modes*) is shown in Figs. 2(a) and 2(c), respectively, as a function of the in-plane wave vector  $\mathbf{k}_\parallel$ . The red curve represents a radiative mode ( $\text{Im } k_{z1} = \text{Im } k_{z2} < 0$ ), while the blue curves represent polaritonic modes ( $\text{Im } k_{z1} = \text{Im } k_{z2} > 0$ ). Both curves are calculated by solving Eq. (12) in the complex-frequency plane. Figures 2(b) and 2(d) similarly show the dispersion and the imaginary part of the frequencies of TM modes [Eq. (13)]. The data of the solid curves, computed assuming the current-sheet and the single-exciton approximations, are compared with the numerical results (dots) obtained by solving Eq. (1) with the transfer matrix method [42]. For these results, the experimental dielectric function of Ref. [43] (parametrized with a set of Lorentzian functions) has been used. The good agreement between the exact and the approximate data confirms that it is possible to use Eqs. (12) and (13) to properly describe the properties of the electromagnetic modes and the transitions among the various regimes that can be reached by varying the parameters of the system.

Our calculations demonstrate the existence of three different TE electromagnetic modes in suspended  $\text{WS}_2$  monolayers: a radiative mode [red curve in Figs. 2(a) and 2(c)] and two polariton modes (blue curves). It is important to note that the situation that we are considering here is very different from the case of ordinary bulk polaritons [25]. In the traditional picture of a polariton, a single light mode is coupled with

a nearly frequency-degenerate single exciton state, giving rise to two hybrid light-matter modes. The energy splitting of the dispersion of the polaritons reflects the amount of coupling. In the present situation, however, the exciton is coupled with a continuum of radiation modes, i.e., the set of light modes indexed by the varying out-of-plane wave vector  $k_{zj} = (\varepsilon_j \omega^2 / c^2 - k_\parallel^2)^{1/2} > 0$  ( $j = 1, 2$ ). The continuum of light modes is indicated by shaded region in Fig. 2. The electromagnetic modes that we discuss in this work represent quasiparticles or resonances in the continuum, which emerge from this collective interaction. In particular, the strength of the interaction with light, whose magnitude is exemplified by the factor  $\Gamma_0^\parallel$ , affects both the dispersion of the modes and the radiative contribution to the dissipation rates in a nontrivial manner.

The radiative mode [red curve in Figs. 2(a) and 2(c)] lies partially inside the continuum of light states. Therefore, it can be excited by incident plane waves with matching in-plane wave vector and it accounts for the exciton peak which is observed in the reflectivity spectra of TMDC monolayers. As it is the case for two-dimensional excitons in the presence of nonradiative dissipation, the dispersion of the radiative mode continues in the region outside the light cone, where direct coupling to incoming and outgoing light waves is not available. This phenomenon reflects the availability of an indirect channel for the conversion of excitons into bulk photons (and vice versa) mediated by nonradiative processes.

The imaginary part of the modal dispersion is shown in Fig. 2(c). The imaginary part of the frequency is directly related to the total decay rate of the mode, i.e., to the loss rate of the excitation energy, according to

$$\gamma_{\text{tot}} = -2 \text{Im}(\omega). \quad (15)$$

As it can be seen from Fig. 2(c), the total decay rate of the radiative mode is always larger than the nonradiative dissipation rate  $\gamma_0$ , reflecting the additional radiative contribution to the losses of the system. For small values of the in-plane momentum, the total decay rate closely follows the perturbative solution

$$\gamma_{\text{tot}} \simeq \gamma_0 + \frac{1}{2} \frac{\omega_0 \Gamma_0^\parallel}{\sqrt{\omega_0^2 - c^2 k_\parallel^2}}, \quad (16)$$

which can be obtained from Eq. (12). The perturbative approximation is not valid in proximity to the light line, where it would actually predict a divergence of the decay rate. On the contrary, the nonperturbative solution, displayed in Fig. 2(c), shows a maximum for the decay rate close to the light line, after which the rate abruptly drops to  $\gamma_0$ , as it is typical for TE-polarized modes [32]. Please note that in all dispersion plots, such as Figs. 2(a) and 2(b), only the shift of the mode frequency with respect to the bare exciton frequency ( $\hbar\omega_0 = 2.014$  eV) is depicted. For instance, all the modes in Fig. 2 have frequencies around 2 eV, about two orders of magnitude larger than the corresponding imaginary parts.

In addition to the radiative mode, the system supports two distinct polariton branches. The polariton branch outside the light cone, indicated with (i) in Fig. 2(a), is a common feature of two-dimensional excitonic systems. The properties of this particular mode for TMDC monolayers have been also described in Ref. [26]. The dispersion of the mode closely

resembles that of surface plasmon polaritons originating at the interface between metals and dielectrics. The second polaritonic branch, indicated with (ii) in Fig. 2(a), is located within the light cone and represents what is typically called an “anomalous” polariton. The existence of this mode is entirely due to the presence of nonradiative dissipation. The existence of dissipation-induced modes in electromagnetic systems has been known for a long time. Two important examples for TM-polarized electromagnetic waves are Brewster and Zenneck modes at the interface of two different optical media. Some of these modes have played an important role in the development of radio engineering at the beginning of the 20th century [44]. Despite being located inside the light cone, a dissipation-induced mode constitutes a fully bound state, i.e., a state with a spatially decaying profile of the field, and it is orthogonal to the modes in the radiative continuum of the system. Similar to other spatially confined modes, it could be visualized with near-field microscopy techniques [32]. It is interesting to note that the dispersion branch of the dissipation-induced polariton abruptly ends close to the edge of the light cone. The exact location of the vanishing point depends on the dissipation level of the system, as it will be discussed in more detail in the following section.

The imaginary part of the polariton dispersion is shown in Fig. 2(c) and it is related to the total decay rate according to Eq. (15). The polariton modes have values of the decay rate which are always lower than the exciton nonradiative dissipation rate  $\gamma_0$ . It can be clearly seen that the end point of the dispersion of the dissipation-induced polariton in Fig. 2(a) corresponds to a value  $\text{Im } \omega = 0$ . The vanishing of the polariton decay rate close to the light line reflects the increase of the light fraction of the mode with respect to the exciton fraction.

The results for TM polarization display a simpler behavior. As shown in Figs. 2(b) and 2(d), there are two modes, whose dispersion curves are very close to the original exciton in both the real and imaginary parts. Since only the in-plane components of the electric field couple with the excitonic mode, light-matter interaction is reduced. As a result, the reversible exchange of energy between the exciton and the radiation field cannot take place and the modes are dominated by the excitonic component. The flatness of the dispersion implies a very low group velocity of the modes. Together with the finite dissipation rate, the low group velocity suggests a physical picture where the modes are strongly localized within a short coherence length.

At this point, we analyze the dispersion of electromagnetic modes in the nonsymmetric case  $\varepsilon_1 \neq \varepsilon_2$ . This is an indispensable extension of our investigation since a common method of preparing TMDC monolayers involves exfoliation on top of a dielectric substrate [1], which we can model with the dielectric constant  $\varepsilon_2$ . For the sake of illustration, we assume  $\varepsilon_1 = 1$  and  $\varepsilon_2 = 2.25$ . The dispersion of the real and imaginary parts of the modes are plotted in Figs. 3(a) and 3(c) and Figs. 3(b) and 3(d) for TE and TM polarizations, respectively.

Similarly to the previous case, it is possible to classify the modes as polaritonic and radiative according to the sign of  $\text{Im } k_z$ . Due to the dielectric function imbalance, the  $z$  components of the wave vector in the upper and lower cladding ( $k_{z1}$  and  $k_{z2}$ ) need to be analyzed independently. The values of the real and imaginary parts of  $k_{z1}$  and  $k_{z2}$  for the TE

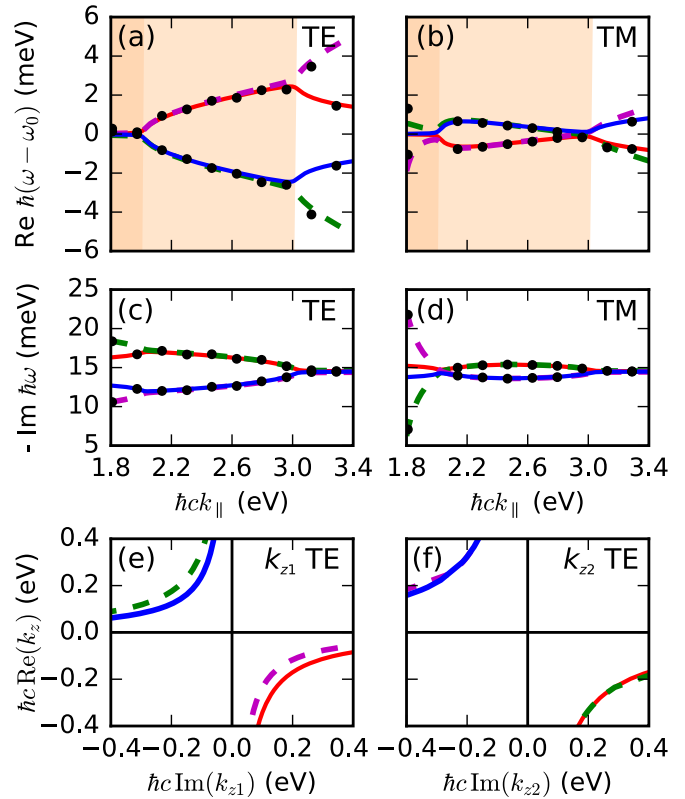


FIG. 3. (a), (b) Real part and (c), (d) imaginary part of the frequency dispersion of the electromagnetic modes of a TMDC monolayer, as a function of the in-plane wave vector. The picture represents the nonsymmetric case  $\varepsilon_1 = 1$  and  $\varepsilon_2 = 2.25$ . All other parameters of the system are the same as in Fig. 2. Red lines: radiative modes; blue lines: polariton modes; dashed purple lines: modes with radiative character in air ( $\varepsilon_1$ ) and polaritonic in the substrate ( $\varepsilon_2$ ); dashed green lines: mixed modes with opposite character, i.e., radiative in the substrate and polaritonic in air. The shaded regions depict the light cones for  $\varepsilon_1$  and  $\varepsilon_2$ . Similarly to Fig. 2, the dots indicate the results of a full-wave numerical calculation with the experimental dielectric constant of WS<sub>2</sub>. (e), (f) Plot of the imaginary part vs the real part of the out-of-plane wave vector  $k_z$  in the  $\varepsilon_1$  (e) and  $\varepsilon_2$  media (f), for the TE modes also shown in (a) and (c).

modes are shown in Figs. 3(e) and 3(f), respectively. The results reveal the existence of a fully radiative mode ( $\text{Im } k_{z1} < 0$ ,  $\text{Im } k_{z2} < 0$ , red curve in Fig. 3) and a fully polaritonic mode ( $\text{Im } k_{z1} > 0$ ,  $\text{Im } k_{z2} > 0$ , blue curve), in analogy with the symmetric case of Fig. 2. Notably, additional anomalous electromagnetic modes of mixed character also appear. These include, on the one hand, a mode with radiative character in the upper layer and polaritonic character in the lower layer ( $\text{Im } k_{z1} < 0$ ,  $\text{Im } k_{z2} > 0$ , purple curves) and, on the other hand, a mode which is polaritonic in the upper layer and radiative in the lower layer ( $\text{Im } k_{z1} > 0$ ,  $\text{Im } k_{z2} < 0$ , green curves). The presence of polaritonic (radiative) modes inside (outside) the corresponding light cone is a dissipation-induced effect that is entirely due to the intrinsic nonradiative decay rate  $\gamma_0$  of the exciton, similarly to the case of the anomalous polariton branch of Fig. 2.

In addition to the increase in the number of modes, the modal dispersion in the nonsymmetric case is qualitatively different

from the symmetric case, especially for TE polarization. Both the real and the imaginary parts of the frequency are weakly affected by the coupling with light. The dispersion of the electromagnetic modes spans a small frequency range around the original exciton frequency of the order of  $\Gamma_0^{\parallel}$ . Although it is still possible to formally classify the modes as polaritons or radiative modes according to the sign of  $\text{Im}k_z$ , the physical interpretation of the behavior of the system is very different than in the symmetric case of Fig. 2. On the one hand, the symmetric system is characterized by the presence of a “traditional” dispersive polaritonic mode [Fig. 2(a)]; on the other hand, in the nonsymmetric case the solutions of the characteristic equation correspond to dispersionless modes, which can be interpreted as weak perturbations over the original exciton. This behavior can be interpreted as a signature of the weak-coupling (perturbative) regime of light-matter interaction.

It is essential to note that the results of this section show that two systems with the same exciton frequency and the same absorption losses can have very different electromagnetic modes, and even be in different coupling regimes, depending on the dielectric function imbalance of the claddings. Consequently, in the next section we will explore the relation between the nonradiative rate and the dielectric function imbalance and their combined effect on the qualitative properties of the electromagnetic modes of the system.

#### IV. PARAMETRIC ANALYSIS OF THE STRONG-COUPLING TRANSITION

In the previous section, we describe the dispersion and decay rate of electromagnetic modes in WS<sub>2</sub> monolayers. Our results show large qualitative differences in the number, properties, and character of the modes for different polarizations and different values of the substrate dielectric constant. In order to understand the origin of these differences, in this section we treat the exciton nonradiative dissipation rate  $\gamma_0$  and the substrate dielectric constant  $\varepsilon_2$  as free parameters, and we explore the variations of the modal dispersion in this parameter space. Moreover, this approach allows us to extend our considerations to other TMDC monolayers in a straightforward way, by choosing the suitable parameters on a case-by-case basis.

The key for interpreting the variations in the polariton dispersion is to describe them in terms of a strong-weak coupling transition [32,34]. It is essential to note, though, that in our case the definition of strong-coupling regime does not require the presence of any form of optical confinement: the phenomena under investigation entirely arise from the interaction between the exciton and the continuum of free-space radiation.

As a starting point, we consider the limiting case of a symmetric configuration of the dielectric constant ( $\varepsilon_1 = \varepsilon_2 = 1$ ) and we assume that only the nonradiative dissipation rate  $\gamma_0$  is varying. This particular situation is the most similar to the case of semiconductor quantum wells and has been extensively investigated in that context [32]. Figure 4(a) displays the dispersion of the real part of the TE polariton frequency as a function of the in-plane wave vector and for selected values of  $\gamma_0$ . For  $\gamma_0 = 0$ , a single polaritonic mode is present, which lies

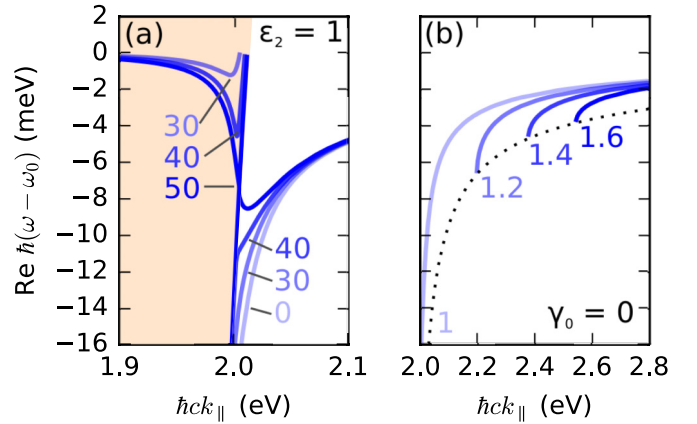


FIG. 4. (a) Dispersion of the real part of the frequency of TE polaritons in TMDC monolayers as a function of the in-plane wave vector. The different curves refer to different values of the nonradiative decay rate of the exciton  $\gamma_0$ , indicated by the labels (the rates are expressed in meV). We assume a symmetric configuration with  $\varepsilon_1 = \varepsilon_2 = 1$ . (b) Dispersion of the polariton modes similarly to (a), but in the assumption of no absorption losses ( $\gamma_0 = 0$ ) and for different values of the substrate dielectric constant  $\varepsilon_2$ , indicated by the labels. The values of the remaining parameters are the same as in Fig. 2.

outside the light cone. This mode represents a fully bound state with  $\text{Im} \omega = 0$ . In this regime, our analysis is fully consistent with previous works on the theory of exciton-polaritons in two-dimensional systems [22–26].

With increasing  $\gamma_0$ , the dispersion of this mode slightly shifts to lower frequencies and closer to the light line. In addition, when the dissipation is larger than the threshold level [32]

$$\gamma_{\text{thr}} = \Gamma_0^{\parallel} / (2\sqrt{\varepsilon_1}), \quad (17)$$

a second dissipation-induced polariton branch (anomalous polariton) emerges inside the light cone. This branch ends at a finite in-plane wave vector, where the imaginary part of the frequency drops to zero. When we increase the nonradiative dissipation, the ending point moves towards the edge of the light cone. At the threshold value

$$\gamma_{\text{tran}} = \frac{3\sqrt{3}}{4 \times 2^{1/3}} \left( \frac{(\Gamma_0^{\parallel})^2 \omega_0}{\varepsilon_1} \right)^{1/3}, \quad (18)$$

the two polaritonic branches intersect. This is the signature of the transition from the strong-coupling regime, when the polaritonic branches are separated, to the weak-coupling regime, when the branches cross each other. The threshold for such a transition is defined in an unambiguous way by the intersection point. In the example of Fig. 4, we calculate a threshold  $\gamma_{\text{tran}} \simeq 43$  meV. The transition to the crossing regime for  $\gamma_0 > \gamma_{\text{tran}}$  is clearly identifiable in the figure when comparing the curves for  $\gamma_0 = 40$  meV with those for  $\gamma_0 = 50$  meV.

As a second case, we consider the situation without nonradiative losses ( $\gamma_0 = 0$ ) and we change the value of the dielectric constant of the substrate with respect to the upper air cladding ( $\varepsilon_2 \neq \varepsilon_1$ ). The dispersion curves of the real part of the polariton frequency for several values of  $\varepsilon_2$  between  $\varepsilon_2 = 1 = \varepsilon_1$  and  $\varepsilon_2 = 1.6$  are depicted in Fig. 4(b). As there

are no absorption losses, the anomalous polariton is indeed not present and the only polariton mode lies outside of the light cone. Interestingly and at variance with the symmetric case, when the polariton dispersion extends all the way to zero frequency in the limit  $k_{\parallel} \rightarrow 0$ , the modal dispersion in the nonsymmetric case is characterized by a finite cutoff. Each cutoff point corresponds to the intersection between the polariton dispersion curve and the substrate material light line  $\omega = ck_{\parallel}/\sqrt{\varepsilon_2}$ . The corresponding frequency of the mode at the cutoff is obtained as

$$\omega_{\text{cutoff}} = \sqrt{\omega_0^2 + \frac{(\Gamma_0^{\parallel})^2}{4(\varepsilon_2 - \varepsilon_1)}} - \frac{\Gamma_0^{\parallel}}{2\sqrt{\varepsilon_2 - \varepsilon_1}}. \quad (19)$$

The cutoff points lie on the curve

$$k_{\parallel} = \sqrt{\varepsilon_1 \frac{\omega^2}{c^2} + \frac{\omega^4 (\Gamma_0^{\parallel})^2}{c^2 (\omega_0^2 - \omega^2)^2}} \quad (\omega < \omega_0), \quad (20)$$

which is shown by the dotted line in Fig. 4(b). As can be observed, the extent of the modal dispersion in frequency space is reduced with the increasing of the dielectric constant imbalance. In the limit  $\varepsilon_2 \gg \varepsilon_1$ , this frequency range can be estimated as

$$\omega - \omega_0 \simeq \frac{\Gamma_0^{\parallel}}{2\sqrt{\varepsilon_2 - \varepsilon_1}}. \quad (21)$$

For instance, in the case  $\varepsilon_1 = 1$  and  $\varepsilon_2 = 2.25$ , the polariton dispersion will be restricted to a frequency range of the order  $\omega - \omega_0 \simeq 0.45\Gamma_0^{\parallel}$ . These results show that the dielectric constant imbalance between the external claddings is a crucial factor in the qualitative dispersion of the polariton modes in TMDC monolayers.

At this point, we can consider the general case of varying both the dissipation rate and the dielectric function imbalance. The situation can be understood in the light of the previous limiting cases. As an example, in Fig. 5(a) we show the dispersion curves of the real part of the polariton frequency for the case  $\gamma_0 = 10$  meV and for selected values of the substrate dielectric function  $\varepsilon_2$ . For low values of the dielectric function imbalance, the situation is analogous to the symmetric case in the strong-coupling regime. It is evident the presence of a traditional polaritonic mode with a definite dispersion spans a large fraction of the frequency space. A further increase of the dielectric function imbalance triggers the transition to the weak-coupling regime. The original polaritonic branch turns into a dispersionless localized mode, reflecting a global loss of coherence and an increase of weight of the excitonic component with respect to the radiative one. In addition to the ordinary polariton, the anomalous dissipation-induced polariton branch originates inside the light cone. The dispersion of the dissipation-induced mode ends at a point in proximity to the air light line, as highlighted by the inset of Fig. 5(a). It is noteworthy that the transition to the weak-coupling regime can be flagged by the intersection of the two modal branches, which takes place above a threshold value for  $\varepsilon_2$ . In the example in the figure, the threshold is  $\varepsilon_2 \simeq 1.36$  [as confirmed by Fig. 5(b)]. The intersection of the branches is clearly identifiable by comparing the  $\varepsilon_2 = 1.3$  and the 1.4 curves.

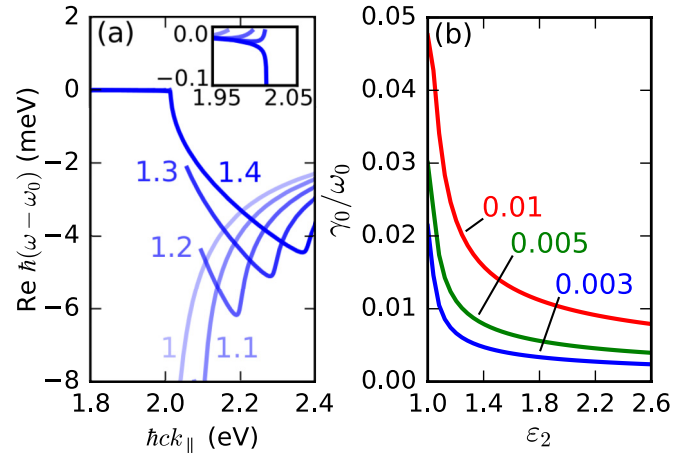


FIG. 5. (a) Dispersion of the real part of the frequency of TE polaritons in TMDC monolayers as a function of  $k_{\parallel}$  for different values of the substrate dielectric constant  $\varepsilon_2$ , indicated by the labels. We assume the exciton nonradiative rate  $\gamma_0 = 10$  meV. The values of the remaining parameters are the same as in Fig. 2. The inset shows a closeup of the dispersion close to the air light line. (b) The critical value of the nonradiative decay rate of the exciton (normalized to the exciton frequency) for the strong-weak coupling transition, as a function of the substrate dielectric constant  $\varepsilon_2$ . The different curves refer to different values of the ratio  $\Gamma_0^{\parallel}/\omega_0$ , indicated by the labels.

As the character of the polaritonic mode drastically changes between the strong-coupling and the weak-coupling regime, it is important to quantify the threshold for such transition. As pointed out by the previous discussion, the weak-coupling transition is a smooth phenomenon, which gradually takes place with varying the parameters of the system. Nevertheless, following the approach of Ref. [32], we define in an unambiguous way a threshold for the transition as the value of the nonradiative dissipation rate at which the ordinary and the anomalous polaritons are exactly degenerate in frequency. Rigorously, we define the threshold as the value of  $\gamma_0$  for which the characteristic equation [Eq. (12), (13), or (14)] possesses a pair of degenerate solutions in the complex-frequency plane at a certain value of  $k_{\parallel}$ . Such threshold depends on both the bare radiative strength  $\Gamma_0^{\parallel}$  and the dielectric function imbalance. The magnitude of the absorption rate that is required to trigger the transition can therefore be very different from the value in Eq. (18), which applies only to the symmetric case.

We have numerically computed the threshold values for the nonradiative dissipation rate and we plot them in Fig. 5(b) as a function of the substrate dielectric constant  $\varepsilon_2$  and for different values of the bare radiative strength  $\Gamma_0^{\parallel}$  (as usual, we assume  $\varepsilon_1 = 1$ ). It becomes clear that the absorption rate greatly reduces with increasing the dielectric constant imbalance. For instance, in the case of a WS<sub>2</sub> monolayer on glass ( $\Gamma_0^{\parallel} = 6$  meV and  $\varepsilon_2 = 2.25$ ), we obtain a critical absorption rate  $\gamma_0 \sim 5$  meV. These considerations explain why in Sec. III we find that in the symmetric case the TE-polarized polariton is in the strong-coupling regime, as opposed to the weak-coupling regime in the nonsymmetric case. Figure 5(b) can be considered as a simple phase diagram for the properties of the polariton modes in TMDC monolayers. The regions above and below each curve represent the weak-coupling

and the strong-coupling regimes, respectively. Every different system, i.e., combination of TMDC material and surroundings, can be identified by a single point on the diagram, as long as the single-exciton approximation remains valid. This allows us to predict the dispersion and the decay rate of TMDC monolayers in a unified way.

## V. CONCLUSIONS

Following the theory of Wannier-Mott excitons in two-dimensional systems, we derive the characteristic equations for the electromagnetic modes supported by TMDC monolayers interposed between two different optical media. The parameters required for modeling the excitonic resonances are derived from an effective dielectric function, which allows for a straightforward comparison with experiments. The same characteristic equation determines both exciton-polaritons and radiative modes, whose electric field is spatially decaying or diverging in the out-of-plane direction, respectively. Exciton-polaritons are spatially confined modes (the electromagnetic analog of bound states) and they originate from the collective interaction between the exciton and the three-dimensional radiation continuum. They are analogous to the exciton-polaritons that are well known from the theory of traditional semiconductor heterostructures. Note that light confinement in these modes has a different origin than in the case of cavity-polaritons, where the exciton is coupled to a single spatially confined radiation mode.

The frequency dispersions and the decay rates of the radiative modes and exciton-polaritons are determined nonperturbatively from the complex-frequency solutions of the characteristic equations. The amount of nonradiative dissipation affects the dispersion of the modes in a profound way. One of the most notable consequences of dissipation is the formation of “anomalous” polaritons, which occurs for sufficiently high nonradiative losses. At variance with “ordinary” polaritons, such anomalous modes lie inside the light cone, despite being dark to far-field radiation. Therefore, they could be experimentally detected with near-field techniques. It is still a question open for future research whether dissipation-induced modes could provide practical benefits for the development of particular optoelectronic devices. Nevertheless, the existence of such modes needs to be taken into account in all kinds of practical applications. For instance, at the very least, dissipation-induced modes represent an additional channel for light to couple with, which cannot be ignored in efficiency or energy balance calculations.

A second important effect of nonradiative dissipation is to trigger a transition between the strong-coupling and the weak-coupling regimes of light-matter interaction. Interestingly, the dissipation threshold for the transition is not fixed, but it strongly depends on the dielectric function imbalance at the two sides of the monolayer. As an illustrative case, we consider a loss rate of the order of 30 meV, compatible with existing experimental data [43]. Our results show that the system is in the strong-coupling regime when suspended in air, yet in the weak-coupling regime when deposited on a dielectric substrate. After the transition to the weak-coupling regime, the ordinary and anomalous polaritonic branches, which are well separated in the strong-coupling regime, merge together

in a single, mostly dispersiveless, electromagnetic mode. This mode bears little resemblance with the original polariton and reflects a strongly localized state with a predominant excitonic component.

We also demonstrate how the threshold for this transition is generally affected by the dielectric constant imbalance. For instance, in our illustrative system, the maximum amount of nonradiative losses compatible with the strong-coupling regime drops from about  $\gamma_0 \simeq 40$  meV to about  $\gamma_0 \simeq 5$  meV when the dielectric function of one of the embedding media changes from  $\varepsilon = 1$  to 2.25. These results demonstrate that a fine control of the optical properties of the claddings is necessary to access the strong-coupling regime for exciton-polaritons. Such a control can be obtained, for instance, by encapsulating the TMDC monolayer into a stack of two-dimensional atomic crystals (such as hexagonal boron nitride), effectively realizing van der Waals heterostructures [3,16].

In summary, the electromagnetic spectrum of TMDC monolayers displays a rich variety of both radiative and polaritonic modes, whose characteristics are strongly dependent on the properties of both the excitonic system and the surrounding environment. Notably, the character of the polaritonic modes is strongly affected by the dielectric constant imbalance at the two sides of the monolayer. By carefully tuning these parameters, it is possible to access the strong-coupling regime of interaction between the excitons and the continuum of electromagnetic radiation.

## ACKNOWLEDGMENTS

F.A. acknowledges financial support from the H2020 Marie Skłodowska-Curie Actions individual fellowship BISTRO-LIGHT (Grant No. 748950). S.H.G. and L.K. acknowledge financial support from the European Research Council (ERC Advanced Grant No. 340438-CONSTANS).

## APPENDIX: OUT-OF-PLANE POLARIZED EXCITONS

In this Appendix, we will present some results for the electromagnetic modes originating from out-of-plane-polarized excitons ( $Z$  modes). The modes can be computed by solving the characteristic equation reported in Eq. (14). First, we consider radiative modes in the perturbative approximation. We assume a solution of the form  $\omega = \tilde{\omega}_0 - i\gamma_{\text{tot}}/2$ . To first order in  $\gamma_0$  and  $\gamma_{\text{rad}}$ , the solution of Eq. (14) is

$$\tilde{\omega}_0^2 = \omega_0^2 + \Delta_0^2, \quad (\text{A1})$$

$$\gamma_{\text{tot}} = \gamma_0 + ck_{\parallel}^2 \Gamma_0^z / (k_{z1}/\varepsilon_1 + k_{z2}/\varepsilon_2), \quad (\text{A2})$$

with  $k_{zj} = (\varepsilon_j \tilde{\omega}_0^2 / c^2 - k_{\parallel}^2)^{1/2}$ . The frequency  $\tilde{\omega}_0$  determines the spectral position of the resonance in far-field optical spectra at non-normal incidence. It is relevant that, in the case of  $Z$  modes, the resonance energy  $\hbar\tilde{\omega}_0$  is not the “bare” exciton energy  $\hbar\omega_0$ , but includes the contribution of the depolarization shift  $\Delta_0^2$ . The exact calculation of the depolarization shift requires the knowledge of the electronic structure of the material [see Eq. (8)] and goes beyond the scope of this work. However, it is important to take into account its effect for an accurate comparison of spectroscopic

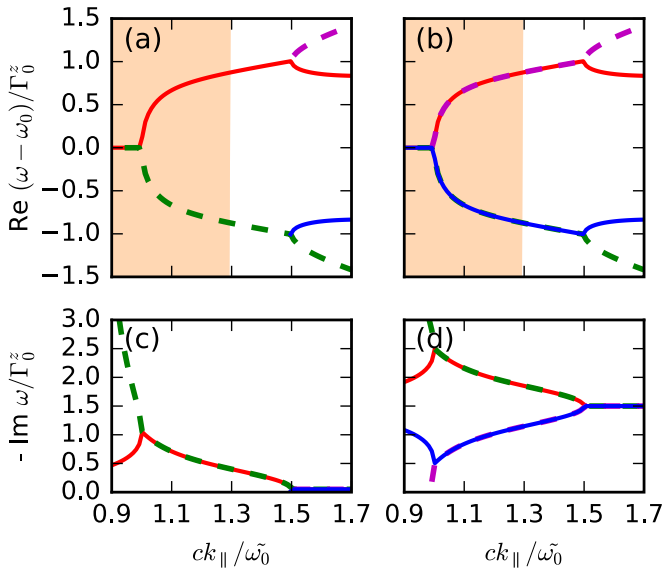


FIG. 6. (a), (b) Real part and (c), (d) imaginary part of the frequency dispersion of the Z modes of a TMDC monolayer, originating from out-of-plane polarized excitons. We assume  $\Gamma_0^z = 10^{-5}\tilde{\omega}_0$ ,  $\varepsilon_1 = 1$ , and  $\varepsilon_2 = 2.25$ . Moreover, (a), (c)  $\gamma_0 = 0.1\Gamma_0^z$ , and (b), (d)  $\gamma_0 = 3\Gamma_0^z$ . Red lines: radiative modes; blue lines: polariton modes; dashed purple lines: radiative modes in the  $\varepsilon_1$  layer and polaritonic in  $\varepsilon_2$ ; dashed green lines: radiative modes in  $\varepsilon_2$  and polaritonic in  $\varepsilon_1$ . The shaded regions depict the light cones for  $\varepsilon_1$  and  $\varepsilon_2$ . All curves are a function of the in-plane wave number  $k_{\parallel}$ .

data with electronic computations. Moreover, Eq. (A2) shows that the radiative part of the decay rate goes to zero for  $k_{\parallel} \rightarrow 0$ , as expected for out-of-plane (TM) polarized modes.

In Fig. 6, we present the dispersion  $\Delta\omega = \omega - \tilde{\omega}_0$  and the imaginary part of the frequencies of electromagnetic modes, extracted from the nonperturbative solutions of Eq. (14). All curves are normalized to the exciton coupling strength  $\Gamma_0^z$ . In Ref. [16], a ratio  $\Gamma_0^z/\Gamma_0^{\parallel} \sim 10^{-4}-10^{-2}$  is estimated for TMDC monolayers. For the sake of illustration, in this example we assume  $\Gamma_0^z = 10^{-5}\tilde{\omega}_0$ . Moreover, we assume a nonsymmetric dielectric function configuration with  $\varepsilon_1 = 1$  and  $\varepsilon_2 = 2.25$ . Figures 6(a) and 6(c) represent the low dissipating case  $\gamma_0 = 0.1\Gamma_0^z$ , whereas Figs. 6(b) and 6(d) correspond to the stronger dissipation  $\gamma_0 = 3\Gamma_0^z$ . Similarly to Fig. 3, we distinguish fully radiative and polaritonic modes (red and blue curves, respectively), and mixed-character modes that are radiative or polaritonic only in one of the two surrounding layers (green and purple curves).

In general, the dispersion of the modes shows very similar features to those that we have previously discussed for in-plane polarized excitons. In Fig. 6(a), which exemplifies the strong-coupling regime of interaction with light, the polariton dispersion (blue curve) is characterized by a finite cutoff, in agreement with the presence of the dielectric function imbalance between the embedding layers [compare Fig. 4(b)]. In Fig. 6(b), on the contrary, the polaritonic dispersion extends all the way into the light cone: as discussed in Sec. IV, this fact is a signature of the weak-coupling regime [compare Fig. 3(a)]. However, the strongly reduced interaction with light of the exciton implies a much lower threshold for the transition between the strong- and weak-coupling regimes than for in-plane polarized excitons. In the example of Fig. 6, we obtain a threshold  $\gamma_0 \simeq 2\Gamma_0^z$ , which is less than 1 meV (assuming  $\tilde{\omega}_0 \simeq 2\text{eV}$ ). This modest coupling with light explains our focus on in-plane polarized electromagnetic modes in the rest of the work.

- [1] K. F. Mak and J. Shan, Photonics and optoelectronics of 2D semiconductor transition metal dichalcogenides, *Nat. Photonics* **10**, 216 (2016).
- [2] K. S. Novoselov, D. Jiang, F. Schedin, T. J. Booth, V. V. Khotkevich, S. V. Morozov, and A. K. Geim, Two-dimensional atomic crystals, *Proc. Natl. Acad. Sci. USA* **102**, 10451 (2005).
- [3] A. K. Geim and I. V. Grigorieva, Van der Waals heterostructures, *Nature (London)* **499**, 419 (2013).
- [4] H. Zeng, J. Dai, W. Yao, D. Xiao, and X. Cui, Valley polarization in MoS<sub>2</sub> monolayers by optical pumping, *Nat. Nanotechnol.* **7**, 490 (2012).
- [5] K. F. Mak, K. He, J. Shan, and T. F. Heinz, Control of valley polarization in monolayer MoS<sub>2</sub> by optical helicity, *Nat. Nanotechnol.* **7**, 494 (2012).
- [6] A. Kormányos, V. Zólyomi, N. D. Drummond, and G. Burkard, Spin-Orbit Coupling, Quantum Dots, and Qubits in Monolayer Transition Metal Dichalcogenides, *Phys. Rev. X* **4**, 011034 (2014).
- [7] T. Karzig, C.-E. Bardyn, N. H. Lindner, and G. Refael, Topological Polaritons, *Phys. Rev. X* **5**, 031001 (2015).
- [8] T. Low, A. Chaves, J. D. Caldwell, A. Kumar, N. X. Fang, P. Avouris, T. F. Heinz, F. Guinea, L. Martin-Moreno, and F. Koppens, Polaritons in layered two-dimensional materials, *Nat. Mater.* **16**, 182 (2016).
- [9] K. F. Mak, C. Lee, J. Hone, J. Shan, and T. F. Heinz, Atomically Thin MoS<sub>2</sub>: A New Direct-Gap Semiconductor, *Phys. Rev. Lett.* **105**, 136805 (2010).
- [10] A. Splendiani, L. Sun, Y. Zhang, T. Li, J. Kim, C.-Y. Chim, G. Galli, and F. Wang, Emerging photoluminescence in monolayer MoS<sub>2</sub>, *Nano Lett.* **10**, 1271 (2010).
- [11] J. S. Ross, S. Wu, H. Yu, N. J. Ghimire, A. M. Jones, G. Aivazian, J. Yan, D. G. Mandrus, D. Xiao, W. Yao, and X. Xu, Electrical control of neutral and charged excitons in a monolayer semiconductor, *Nat. Commun.* **4**, 1474 (2013).
- [12] A. Chernikov, T. C. Berkelbach, H. M. Hill, A. Rigosi, Y. Li, O. B. Aslan, D. R. Reichman, M. S. Hybertsen, and T. F. Heinz, Exciton Binding Energy and Nonhydrogenic Rydberg Series in Monolayer WS<sub>2</sub>, *Phys. Rev. Lett.* **113**, 076802 (2014).
- [13] M. M. Ugeda, A. J. Bradley, S.-F. Shi, F. H. da Jornada, Y. Zhang, D. Y. Qiu, W. Ruan, S.-K. Mo, Z. Hussain, Z.-X. Shen, F. Wang, S. G. Louie, and M. F. Crommie, Giant bandgap renormalization and excitonic effects in a monolayer transition metal dichalcogenide semiconductor, *Nat. Mater.* **13**, 1091 (2014).
- [14] K. He, N. Kumar, L. Zhao, Z. Wang, K. F. Mak, H. Zhao, and J. Shan, Tightly Bound Excitons in Monolayer WSe<sub>2</sub>, *Phys. Rev. Lett.* **113**, 026803 (2014).

- [15] B. Zhu, X. Chen, and X. Cui, Exciton binding energy of monolayer WS<sub>2</sub>, *Sci. Rep.* **5**, 9218 (2015).
- [16] G. Wang, C. Robert, M. M. Glazov, F. Cadiz, E. Courtade, T. Amand, D. Lagarde, T. Taniguchi, K. Watanabe, B. Urbaszek, and X. Marie, In-Plane Propagation of Light in Transition Metal Dichalcogenide Monolayers: Optical Selection Rules, *Phys. Rev. Lett.* **119**, 047401 (2017).
- [17] Q. H. Wang, K. Kalantar-Zadeh, A. Kis, J. N. Coleman, and M. S. Strano, Electronics and optoelectronics of two-dimensional transition metal dichalcogenides, *Nat. Nanotechnol.* **7**, 699 (2012).
- [18] F. Alharbi, J. D. Bass, A. Salhi, A. Alyamani, H.-C. Kim, and R. D. Miller, Abundant non-toxic materials for thin film solar cells: Alternative to conventional materials, *Renewable Energy* **36**, 2753 (2011).
- [19] Z. Yin, H. Li, H. Li, L. Jiang, Y. Shi, Y. Sun, G. Lu, Q. Zhang, X. Chen, and H. Zhang, Single-layer MoS<sub>2</sub> phototransistors, *ACS Nano* **6**, 74 (2011).
- [20] H. S. Lee, S.-W. Min, Y.-G. Chang, M. K. Park, T. Nam, H. Kim, J. H. Kim, S. Ryu, and S. Im, MoS<sub>2</sub> nanosheet phototransistors with thickness-modulated optical energy gap, *Nano Lett.* **12**, 3695 (2012).
- [21] G. Eda, H. Yamaguchi, D. Voiry, T. Fujita, M. Chen, and M. Chhowalla, Photoluminescence from chemically exfoliated MoS<sub>2</sub>, *Nano Lett.* **11**, 5111 (2011).
- [22] V. M. Agranovich and O. A. Dubovskii, Effect of retarded interaction on the exciton spectrum in one-dimensional and two-dimensional crystals, *Zh. Eksp. Teor. Fiz. Pis'ma Red.* **3**, 345 (1966) [*JETP Lett.* **3**, 223 (1966)].
- [23] M. Nakayama, Theory of the excitonic polariton of the quantum well, *Solid State Commun.* **55**, 1053 (1985).
- [24] L. C. Andreani and F. Bassani, Exchange interaction and polariton effects in quantum-well excitons, *Phys. Rev. B* **41**, 7536 (1990).
- [25] L. C. Andreani, Exciton-polaritons in bulk semiconductors and in confined electron and photon systems, in *Strong Light-Matter Coupling: From Atoms to Solid-State Systems*, edited by A. Auffèves, D. Gerace, M. Richard, S. Portolan, M. de França Santos, L. C. Kwek, and C. Miniatura (World Scientific, Singapore, 2014), Chap. 2, p. 37.
- [26] J. B. Khurgin, Two-dimensional exciton-polariton-light guiding by transition metal dichalcogenide monolayers, *Optica* **2**, 740 (2015).
- [27] X. Liu, T. Galfsky, Z. Sun, F. Xia, E. c. Lin, Y.-H. Lee, S. Kéna-Cohen, and V. M. Menon, Strong light-matter coupling in two-dimensional atomic crystals, *Nat. Photonics* **9**, 30 (2014).
- [28] Y.-J. Chen, J. D. Cain, T. K. Stanev, V. P. Dravid, and N. P. Stern, Valley-polarized exciton-polaritons in a monolayer semiconductor, *Nat. Photonics* **11**, 431 (2017).
- [29] L. Novotny and B. Hecht, *Principles of Nano-Optics* (Cambridge University Press, Cambridge, UK, 2012).
- [30] H. F. Hess, E. Betzig, T. D. Harris, L. N. Pfeiffer, and K. W. West, Near-field spectroscopy of the quantum constituents of a luminescent system, *Science* **264**, 1740 (1994).
- [31] M. Kohl, D. Heitmann, P. Grambow, and K. Ploog, Luminescence of quantum-well exciton polaritons from microstructured Al<sub>x</sub>Ga<sub>(1-x)</sub>As – GaAs multiple quantum wells, *Phys. Rev. B* **37**, 10927 (1988).
- [32] C. Creatore and A. L. Ivanov, Strong and weak coupling limits in optics of quantum well excitons, *Phys. Rev. B* **77**, 075324 (2008).
- [33] F. Alpeggiani and L. C. Andreani, Semiclassical theory of multisubband plasmons: Nonlocal electrodynamics and radiative effects, *Phys. Rev. B* **90**, 115311 (2014).
- [34] S. Huppert, A. Vasanelli, G. Pegolotti, Y. Todorov, and C. Sirtori, Strong and ultrastrong coupling with free-space radiation, *Phys. Rev. B* **94**, 155418 (2016).
- [35] K. Andersen, S. Latini, and K. S. Thygesen, Dielectric genome of van der Waals heterostructures, *Nano Lett.* **15**, 4616 (2015).
- [36] R. Atanasov, F. Bassani, and V. M. Agranovich, Mean-field polariton theory for asymmetric quantum wells, *Phys. Rev. B* **49**, 2658 (1994).
- [37] C. Zhang, H. Wang, W. Chan, C. Manolatu, and F. Rana, Absorption of light by excitons and trions in monolayers of metal dichalcogenide MoS<sub>2</sub>: Experiments and theory, *Phys. Rev. B* **89**, 205436 (2014).
- [38] P. Dey, J. Paul, Z. Wang, C. E. Stevens, C. Liu, A. H. Romero, J. Shan, D. J. Hilton, and D. Karaiskaj, Optical Coherence in Atomic-Monolayer Transition-Metal Dichalcogenides Limited by Electron-Phonon Interactions, *Phys. Rev. Lett.* **116**, 127402 (2016).
- [39] M. Selig, G. Berghäuser, A. Raja, P. Nagler, C. Schüller, T. F. Heinz, T. Korn, A. Chernikov, E. Malic, and A. Knorr, Excitonic linewidth and coherence lifetime in monolayer transition metal dichalcogenides, *Nat. Commun.* **7**, 13279 (2016).
- [40] J. P. Echeverry, B. Urbaszek, T. Amand, X. Marie, and I. C. Gerber, Splitting between bright and dark excitons in transition metal dichalcogenide monolayers, *Phys. Rev. B* **93**, 121107 (2016).
- [41] W. C. Tait, Quantum theory of a basic light-matter interaction, *Phys. Rev. B* **5**, 648 (1972).
- [42] A. Yariv and P. Yeh, *Photonics: Optical Electronics in Modern Communications*, 6th ed. (Oxford University Press, Oxford, UK, 2006).
- [43] Y. Li, A. Chernikov, X. Zhang, A. Rigosi, H. M. Hill, A. M. van der Zande, D. A. Chenet, E.-M. Shih, J. Hone, and T. F. Heinz, Measurement of the optical dielectric function of monolayer transition-metal dichalcogenides: MoS<sub>2</sub>, MoSe<sub>2</sub>, WS<sub>2</sub>, and WSe<sub>2</sub>, *Phys. Rev. B* **90**, 205422 (2014).
- [44] P. Halevi, Polaritons at the interface between two dielectric media, in *Electromagnetic surface modes*, edited by A. D. Boardman (Wiley, Chichester, UK, 1982), Chap. 7, p. 249.